PROCEEDINGS OF SPIE

SPIEDigitalLibrary.org/conference-proceedings-of-spie

Geometic image formation for target identification in multi-energy computed tomography

Brian H. Tracey
Eric L. Miller

SPIE.

Geometric image formation for target identification in multi-energy computed tomography

Brian H. Tracey and Eric L. Miller

Dept. of Electrical and Computer Engineering, Tufts University, Medford, MA, USA.

ABSTRACT

Recent years have seen growing interest in exploiting dual- and multi-energy measurements in computed tomography (CT) in order to characterize material properties as well as object geometry. Materials characterization is performed by decomposing the scene into constitutive basis functions, such as Compton and photoelectric scattering functions used here. While well motivated physically, the joint recovery of the spatial distribution of photoelectric and Compton properties is severely complicated by the lack of sensitivity in the data to photoelectric variations. Moreover, while we have prior knowledge of Compton and photoelectric coefficients for materials of interest, this prior knowledge is imperfect and the true physical properties may assume a range of values. We propose a model-based iterative approach which accounts for the polyenergetic nature of computed tomography and includes patch based regularization terms to stabilize inversion of photoelectric coefficients. Further, we use a level set-based method to provide high spatial resolution for materials of interest, allowing initial estimates of material properties to be adjusted within a user-specified range. Initial results indicate that this approach is promising for future dual- and multi-energy CT systems with enhanced material characterization capabilities, for use in airport baggage screening and potentially in medical imaging.

Keywords: Computed Tomography, X-ray, CT, dual-energy, image formation, level set

1. INTRODUCTION

Typical Computed Tomography (CT) systems provide an image of the spatially varying X-ray absorption within the object being imaged. While CT is a key imaging modality in medical, security, and non-destructive testing applications, this approach provides minimal information on material properties. In recent years there has been substantial interest in dual- or multi-energy CT systems, in which measurements are made either with differing X-ray energy spectra,[1] or using energy-resolving detectors.[2] By exploiting the energy-dependence of X-ray attenuation, these systems can provide additional, valuable information regarding object material properties.

In previous work,[3] our group developed an approach to geometric image formation for dual-energy CT reconstruction that exploited prior knowledge of the properties of materials of interest. This approach was designed specifically for airport luggage screening applications, where the materials being scanned may vary greatly (as opposed to medical CT, where the tissue properties in the human body are relatively constrained). In this approach, the object was decomposed into Compton and photoelectric coefficient images, as described below, and these images were further separated into background and foreground domains, with objects of interest captured in the foreground. A key challenge in this or other dual-energy image formation approaches is regularization of the photoelectric image, which is typically much more difficult to reliably estimate than the Compton image.[3,4]

In this paper we continue and further extend this work. Our contributions are as follows: 1) we demonstrate that patch-based non-local means (NLM) regularization terms can provide an effective method for stabilizing reconstruction of the photoelectric image; 2) we develop a computationally cheaper, decoupled level set approach to estimating the geometry of foreground objects; and 3) we demonstrate the above techniques on simulated data that mimics a commercial scanner.

The structure of this paper is as follows. In Section 2, we review the physical model used for polyenergetic, dual-energy CT image formation, and describe the inverse problem being solved. In Section 3, we outline the

Further author information: (Send correspondence to B.H.T.)
B.H.T.: E-mail: btracey@eecs.tufts.edu, Telephone: 1 617 627 6424
E.L.M.: E-mail: elmiller@eecs.tufts.edu, Telephone: 1 617 627 3220

Algorithms for Synthetic Aperture Radar Imagery XX, edited by Edmund Zelnio, Frederick D. Garber, Proc. of SPIE Vol. 8746, 87460T · © 2013 SPIE
CCC code: 0277-786X/13/$18 · doi: 10.1117/12.2020668

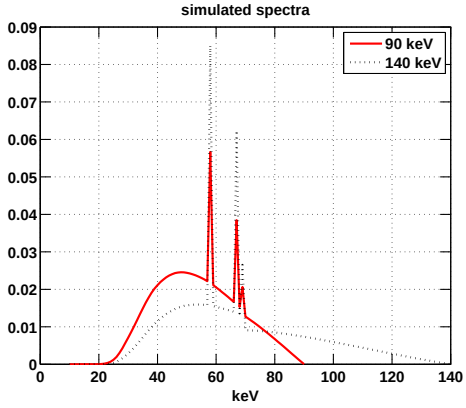

Figure 1. Normalized X-ray energy spectra for high- and low-energy scans

method used to estimate the background Compton and photoelectric (PE) images, with a particular emphasis on use of non-local means methods to regularize the photoelectric image. In Section 4 we present the level set method used to find the foreground object, i.e. material of interest. In Section 5 we present simulation results, and conclude in Section 6.

2. PROBLEM STATEMENT

Typical X-ray sources used in CT applications generate an energy spectra roughly between 20KeV and 140KeV[5] (see Figure 1 for typical spectra from our dual-energy studies). In this energy range X-ray attenuation physics are dominated by Compton scatter and photoelectric absorption. We model these phenomena as a product of energy- and material-dependent terms[4] as follows

$$\mu(x,y,E) = c(x,y) f_{KN}(E) + p(x,y) f_p(E) \tag{1}$$

where $\mu(x,y,E)$ is the total attenuation and $c(x,x)$ and $p(x,y)$ are the material dependent Compton scatter and photoelectric absorption coefficients respectively. The quantity f_{KN} is the Klein-Nishina cross section for Compton scattering which is given as:

$$f_{KN}(\alpha) = \frac{1+\alpha}{\alpha^2}\left[\frac{2(1+\alpha)}{1+2\alpha} - \frac{1}{\alpha}\ln(1+2\alpha)\right] \quad + \frac{1}{2\alpha}\ln(1+2\alpha) - \frac{1+3\alpha}{(1+2\alpha)^2} \tag{2}$$

where $\alpha = E/510.95\text{KeV}$. Lastly, f_p approximates the energy dependency of the Photoelectric absorption and given as $f_b = E^{-3}$. The units of $\mu(x,y,E)$ and $c(x,x)$ are cm^{-1}, while $p(x,y)$ has units of $KeVcm^{-1}$.

Here we will regard Compton and photoelectric coefficients as two different images to be reconstructed. In applications where the materials being imaged are well characterized it may be preferable to instead use basis functions capturing these materials, rather than Compton and photoelectric (for example, bone and tissue in medical imaging). However, the Compton / PE decomposition, being motivated by the X-ray physics, is quite general and is well suited to the luggage screening application.[4] After image formation, material identification can be based on the estimated Compton and photoelectric coefficient images.

A further aspect of our approach is the separation of the domain into *foreground* and *background*, modeled as piecewise constant objects of interest on an unknown background. For a domain $\Omega \subset \mathcal{D}$ which represents the support of the objects of interest, the characteristic function $\chi(x,y)$ is defined as

$$\chi(x,y) = \begin{cases} 1, & \text{if } (x,y) \in \Omega \\ 0, & \text{if } (x,y) \in \mathcal{D}\backslash\Omega. \end{cases} \tag{3}$$

(we describe the calculation of $\chi(x,y)$ in more detail in Section 4). Now, the Compton and photoelectric images can be written as

$$c(x,y) = \chi(x,y) c_f + [1 - \chi(x,y)]\, c_b(x,y) \tag{4}$$

and

$$p(x,y) = \chi(x,y)p_f + [1-\chi(x,y)]\, p_b(x,y). \tag{5}$$

Here c_f and p_f are the Compton scatter and photoelectric absorption coefficients of the foreground (object of interest) and are assumed to be constant, while $c_b(x,y)$ and $p_b(x,y)$ are the background images.

In practice, we solve for the Compton and photoelectric images on a discretized domain. Unwrapping $c_b(x,y)$, $p_b(x,y)$ and $\chi(x,y)$ lexicographically into vectors $\mathbf{c_b}$, $\mathbf{p_b}$, and $\boldsymbol{\chi}$, the vectorized Compton and photoelectric images can be written as

$$\mathbf{c} = \boldsymbol{\chi}\, c_f + (\mathbf{I} - diag\,(\boldsymbol{\chi}))\, \mathbf{c_b} \tag{6}$$

and

$$\mathbf{p} = \boldsymbol{\chi}\, p_f + (\mathbf{I} - diag\,(\boldsymbol{\chi}))\, \mathbf{p_b} \tag{7}$$

where $diag\,(\boldsymbol{\chi})$ is a diagonal matrix whose entries are the values of the unwrapped characteristic function $\boldsymbol{\chi}$.

The CT system samples these images by measuring attenuation along ray-paths connecting multiple sources and receivers. This measurement process is captured in a *system matrix* $\mathbf{A}$, which is the mapping from image pixels to CT raypaths. The system matrix can be computed using the Radon transform if parallel beam projections are performed, or can be computed using ray-trace[6]or projection methods[7] given knowledge of the system geometry. In either case, we assume that a single-energy scan yields a set of M measurements. The process is repeated for low and high energy source spectra to create a modeled data vector $\mathbf{m}^T = [\mathbf{m}_L^T, \mathbf{m}_H^T]$ which consists of $2M$ elements. As will be described in subsequent sections, we expand the background images $c_b(x,y)$ and $p_b(x,y)$ as well as the characteristic function as a combination of basis functions. Collecting the basis coefficients as well as the foreground properties c_f and p_f into a parameter vector $\boldsymbol{\theta}$, the ith measurement for the low energy scan is written as:

$$[\mathbf{m}_L(\boldsymbol{\theta})]_i = -\ln \frac{[\mathbf{Y}_L(\boldsymbol{\theta})]_i}{Y_{0,L}} \tag{8}$$

and similarly for the high-energy scan data, $[\mathbf{m}_H]_i$. The set of all such measurements for one scan is known as a *sinogram*.

We model the measurements $\mathbf{Y}_L$ and $\mathbf{Y}_H$ as vectors of additive Poisson-Gaussian random variables given as

$$[\mathbf{Y}_L(\boldsymbol{\theta})]_i = \text{Poisson}\left\{[\overline{\mathbf{Y}}_L(\boldsymbol{\theta})]_i\right\} + \text{Normal}(0, \sigma_{e,L}) \tag{9}$$

with $[\mathbf{Y}_H(\boldsymbol{\theta})]_i$ being similar. The Poisson variables account for the X-ray counting statistics, while the Gaussian terms captures detector electronics noise. The corresponding means $[\overline{\mathbf{Y}}_L]_i$ and $[\overline{\mathbf{Y}}_H]_i$ are given as

$$\begin{aligned} [\overline{\mathbf{Y}}_L]_i &= \int S_L(E)\exp\big(-f_{KN}(E)\mathbf{A}_{i*}\mathbf{c}(\boldsymbol{\theta}) && (10)\\ &\quad -f_p(E)\mathbf{A}_{i*}\mathbf{p}(\theta)\big)\mathrm{d}E && (11)\end{aligned}$$

and

$$\begin{aligned} [\overline{\mathbf{Y}}_H]_i &= \int S_H(E)\exp\big(-f_{KN}(E)\mathbf{A}_{i*}\mathbf{c} && (12)\\ &\quad -f_p(E)\mathbf{A}_{i*}\mathbf{p}\big)\mathrm{d}E. && (13)\end{aligned}$$

Here, $\mathbf{A}_{i*}$ is the i^{th} row of $\mathbf{A}$, and $S_L(E)$ and $S_H(E)$ correspond to normalized low and high energy X-ray spectra which are shown in Fig. 1. Note that the data will also include scatter contributions not captured above. However, we neglect scatter here, as scatter corrections can be applied to measured data in pre-processing.[8]

The discussion so far in this section has described our mathematical forward model. To invert for the desired images, we stack the multi-energy CT observations into a data vector $\mathbf{y}$ (for the dual-energy case, $\mathbf{y}^T = [\mathbf{y}_L^T, \mathbf{y}_H^T]$). We then seek a solution that minimizes a sum of data fidelity and regularization terms:

$$\arg\min_{\boldsymbol{\theta}} F(\boldsymbol{\theta}) = \frac{1}{2}\left(\mathbf{y} - \mathbf{m}(\boldsymbol{\theta})\right)\boldsymbol{\Sigma}\left(\mathbf{y} - \mathbf{m}(\boldsymbol{\theta})\right)^T + R_{BG}(\boldsymbol{\theta}) + R_{FG}(\boldsymbol{\theta}) \tag{14}$$

where $\mathbf{\Sigma}$ is the noise covariance matrix,[9] and R_{BG} and R_{FG} are background and foreground regularization terms, respectively.

In previous work, Semerci *et al.*[3] treated a coupled problem in which both foreground and background estimates are estimated jointly. Here we instead approach background and foreground estimation as decoupled problems, describing background image estimation in Section 3 and foreground estimation in Section 4. Our motivation for decoupling the foreground and background problems is primarily computational, as we are applying the algorithms to much larger systems than those previously studied.

3. BACKGROUND ESTIMATION

Here we describe estimation of the background Compton and photoelectric images. To reduce computation and to stabilize under-determined CT problems, we express the two images in terms of a common basis function $\mathbf{B}$ (note that if desired, pixel-wise reconstruction can be done by setting $\mathbf{B} = \mathbf{I}$). The images are then parameterized using coefficient vectors as follows:

$$\begin{aligned} \mathbf{c}_b &= \mathbf{B}\beta_{\mathbf{c}} \\ \mathbf{p}_b &= \mathbf{B}\beta_{\mathbf{p}} \end{aligned} \tag{15}$$

where the two images $\mathbf{c}$ and $\mathbf{p}$ are lexicographically unwrapped into a vector of length N, the coefficient vectors β are of length N_R, and the basis $\mathbf{B}$ is of size $N \times N_R$.

During recovery, we collect the background unknowns into a vector:

$$\boldsymbol{\theta}_{BG} = [\boldsymbol{\beta_c}^T \boldsymbol{\beta_p}^T]^T \tag{16}$$

and seek to minimize the quantity

$$\arg\min_{\boldsymbol{\theta}_{BG}} F(\boldsymbol{\theta}_{BG}) = \frac{1}{2}\left(\mathbf{y} - \mathbf{m}(\boldsymbol{\theta}_{BG})\right)\mathbf{\Sigma}\left(\mathbf{y} - \mathbf{m}(\boldsymbol{\theta}_{BG})\right)^T + R_{NLM}(\boldsymbol{\beta_p} \mid \boldsymbol{\beta_c}) \tag{17}$$

which is a simplified version of Eq. 14 including background only. We note that the modeled data also depends on knowledge of the source spectrum and system matrix, although these are assumed known and therefore are not shown explicitly.

The R_{NLM} term regularizes the PE image based on patch-wise similarities (NLM weights) found from the Compton image. Here we are adapting a regularization approach originally proposed by Buades *et al*[10] and recently applied to iterative PET inversion.[11] The concept behind this regularization is that in some applications, a stable 'reference' image is available to guide the inversion of a less stably estimated image with similar geometry. For multi-energy CT we can exploit the relative stability of the inverted Compton image and use it as a reference image to guide photoelectric coefficient inversion. The geometry from the reference image is captured by calculating patch-wise similarity weights from the reference, as found in the non-local means (NLM) denoising algorithm, and using these weights to smooth the noisier image. We therefore define a regularization term:

$$R_{nlm} = \lambda_{NLM} \int \left(p_b(x,y) - NL^{(C)} p_b(x,y)\right)^2 dx\, dy \tag{18}$$

where $NL^{(C)}$ represents non-local means averaging done using weights calculated from the Compton image, used as a reference. The discrete representation of this regularizer is found by summing over pixels j

$$\begin{aligned} R_{nlm} &= \lambda_{NLM} \sum_j \left(\mathbf{p}_b(j) - NL^{(C)}\mathbf{p}_b(j)\right)^2 \\ &= \lambda_{NLM} \sum_j \left(\mathbf{p}_b(j) - \frac{1}{Z_j^{(C)}} \sum_{k \in N_j} w_{jk}^{(C)} \mathbf{p}_b(k)\right)^2 \equiv \lambda_{NLM} \sum_j \delta_j^2 \end{aligned} \tag{19}$$

where δ_j has been defined as pixels in the 'difference image', and superscript 'C' indicates quantities calculated from the Compton image. The weights $w_{jk}^{(C)}$ are found using standard methods from the NLM literature.[10,12] As discussed below, we use an iterative solution method and compute weights at each iteration based on the previous iteration's Compton estimate. The success of the NLM regularization approach depends on reasonable choice of smoothing parameters assumed in the denoising process. Fortunately, a wide variety of approaches for selecting NLM and for reducing sensitivity to parameter selection have been developed (see[12] and references therein).

Our group's previous work[3] instead used an edge-correlation regularization term to stabilize the photoelectric image. As compared to this previous approach, the NLM regularizer has two key advantage: a) it helps to reduce noise artifacts in the recovered image, by building a denoising step into the inversion; b) it is convex, allowing us to consider recently developed convex solution approaches.

Levenburg-Marquart solution

In previous work,[3,9] it was demonstrated that a Levenburg-Marquart solution provides an efficient means of solving the inverse problem in Eq. 14. The Levenburg-Marquart approach requires calculation of the Jacobian $\mathbf{J}$ capturing the sensitivity of model output to all parameters, as well as calculation of terms of the form $\mathbf{J}^T\mathbf{J}\mathbf{x}$. Expressions for the Jacobian for terms other than the NLM regularizer were given previously.[9] For the results shown below we simultaneously update all values of $\boldsymbol{\theta}_{BG} = [\boldsymbol{\beta_c}^T \boldsymbol{\beta_p}^T]^T$ on each iteration, and stop iterating when changes in $\|\boldsymbol{\theta}_{BG}\|_2^2$ fall below a threshold value.

Because our problem sizes are much larger than those examined in,[3,9] explicit storage of $\mathbf{J}$ and $\mathbf{J}^T\mathbf{J}$ is not possible. Similar to other authors,[13] we reduce memory storage by computing $\mathbf{J}^T\mathbf{J}\mathbf{x}$ in two steps (first, $\mathbf{y} = \mathbf{J}\mathbf{x}$, then $\mathbf{J}^T\mathbf{y}$). We also reduce memory requirements by reformulating the Jacobian terms as products of stored vectors with the system matrix, then computing $\mathbf{J}$ and $\mathbf{J}^T$ on-the-fly as needed. Further, we exploit the fact that we are using a basis function and store $\mathbf{K} = \mathbf{B}\mathbf{A}$, rather than storing the system matrix $\mathbf{A}$ directly. While these steps allow us to consider real-world problem sizes (results below use $1024x720$ raypaths), we note that if needed, the system matrix can be calculated on demand, giving a matrix-free iterative method.[13]

As the NLM regularizer was not included in our previous work,[9] we need to calculate the Jacobian of this regularizer. If a pixel-wise solution is used, the i^{th} element of the Jacobian with respect to the photoelectric image is

$$J_{nlm}(i) = \frac{\partial R_{nlm}}{\partial \mathbf{p}_b(i)} = 2\left(\delta_i - \sum_j \delta_j \frac{w_{ij}^{(C)}}{Z_j^{(C)}})\right) \tag{20}$$

Here, note that the second term is equal to a NLM-smoothed version of the difference image δ_j (defined in Eq. 19). Thus, it can easily be found by calling the NLM code twice, using the Compton image from the previous iteration in both cases to calculate weights. Because we use the previous iteration's Compton image, R_{NLM} does not depend on the current Compton estimate, so $\partial R_{nlm}/\partial \mathbf{c}_b = 0$.

As discussed above, we generally express the images as a sum of basis functions. From Eq. 16, the jth element is found by multiplying by the jth row of B:

$$\mathbf{p}_b(j) = \mathbf{B}_{[j]}\boldsymbol{\beta}_p \tag{21}$$

Thus we rewrite the regularizer as

$$R_{nlm} = \sum_j \left(\mathbf{B}_{[j]}\boldsymbol{\beta}_p \left(1 - \frac{w_{jj}^{(C)}}{Z_j^{(C)}}\right) - \frac{1}{Z_j^{(C)}} \sum_{k\neq j, k\in N_j} w_{jk}^{(C)} \mathbf{B}_{[k]}\boldsymbol{\beta}_p\right)^2$$

When taking the derivative with respect to the *ith* coefficient, we can use the chain rule:

$$\begin{aligned}\frac{\partial R_{nlm}}{\partial \boldsymbol{\beta}_p(i)} &= \left(\frac{\partial R_{nlm}}{\partial \mathbf{p}_b}\right)^T \frac{\partial \mathbf{p}_b}{\partial \boldsymbol{\beta}_p(i)} \\ &= \sum_l \frac{\partial R_{nlm}}{\partial \mathbf{p}_b(l)} \frac{\partial \mathbf{p}_b(l)}{\partial \boldsymbol{\beta}_p(i)} \\ &= \sum_l \frac{\partial R_{nlm}}{\partial \mathbf{p}_b(l)} \mathbf{B}_{[k,l]}\end{aligned} \tag{22}$$

which is just the pixel-based Jacobian times the basis function matrix. Note that if we move back to the pixel basis, then $\mathbf{B} \Rightarrow \mathbf{I}$, $\boldsymbol{\beta}_p \Rightarrow \mathbf{p}_b$, and the equation above reverts to the result for the pixel-based Jacobian.

4. FOREGROUND OBJECT ESTIMATION

The previous section described an approach to estimating background Compton and photoelectric coefficients, namely the quantities $c_b(x,y)$ and $p_b(x,y)$ from Eqs. 4 and 5. We now seek to estimate the other terms in the image, namely the characteristic function χ which describes the location of an object of interest, and the exact Compton and photoelectric coefficients for the object.

In estimating χ, we make use of level set concepts, and define the characteristic function $\chi(x,y)$ as the zero level set of an Lipschitz continuous object function $\mathcal{O} : \mathcal{D} \longrightarrow \mathbb{R}$ such that $\mathcal{O}(x,y) > 0$ in Ω, $\mathcal{O}(x,y) < 0$ in $\Omega \backslash \mathcal{D}$ and $\mathcal{O}(x,y) = 0$ in $\partial\Omega$. Using $\mathcal{O}(x,y)$, $\chi(x,y)$ is written as

$$\chi(x,y) = H(\mathcal{O}(x,y)) \tag{23}$$

where H is the step function. In practice, H_ϵ and its derivative δ_ϵ which are smooth approximations of the step function and Dirac delta function respectively, are used.[14] For $\epsilon \in \mathbb{R}^+$ we have the following:

$$H_\epsilon(x) = \begin{cases} \frac{1}{2}\left(1 + \frac{2}{\epsilon} + \frac{1}{\pi} sin\left(\frac{\pi x}{\epsilon}\right)\right) & \text{if } |x| \leq \epsilon \\ 1 & \text{if } x > \epsilon \\ 0 & \text{if } x < -\epsilon \end{cases} \tag{24}$$

and

$$\delta_\epsilon(x) = \begin{cases} \frac{1}{2\epsilon}\left(1 + sin\left(\frac{\pi x}{\epsilon}\right)\right) & \text{if } |x| \leq \epsilon \\ 0 & \text{otherwise.} \end{cases} \tag{25}$$

Level set representation of regions is widely used in image processing[15] as well as image formation.[16] In our approach, we use a parametric level set (PaLS) approach[17] which represents the object function $\mathcal{O}(x,y)$ parametrically using a predefined basis set as

$$\mathcal{O}(x,y) = \sum_{i=1}^{L} a_i b_i(x,y) \tag{26}$$

where a_i's are the weight coefficients and $b_i(x,y)$ are the functions which belong to the basis set of $\mathcal{B}_{fg} = \{b_1, b_2, \ldots, b_L\}$. The PaLS problem then is reduced to the determination of a set of expansion coefficients. This approach eliminates the requirement of a reinitialization process as well as implementation of narrow band methods which are essential for the standard level-set curve evolution approaches, while preserving well known properties of the level set approach of such as topological flexibility and capability to represent multiple objects.[14] Here, we use exponential radial basis functions (RBF's) for the object function basis set $\{b_i(x,y) | i = 1, \ldots, L\}$. Exponential RBFs are defined as

$$b_i(\mathbf{r}) = \exp\left(-\frac{\|\mathbf{r} - \mathbf{r}_i\|^2}{\sigma^2}\right). \tag{27}$$

Here $\mathbf{b}_i : \mathcal{R}^2 \rightarrow \mathcal{R}$ is the i$^{\text{th}}$ RBF, $\mathbf{r} = (x,y)$, $\mathbf{r}_i$ is the center of the i$^{\text{th}}$ basis function and σ is the width which is fixed for all RBFs in the basis set. Once the number of elements in the basis set is determined σ's can be determined by a least squares fit to images with simple geometries.[18]

As noted previously, we assume the material of interest has constant material properties. Thus the parameters of our foreground model (PaLS coefficients, foreground Compton coefficient, and foreground photoelectric coefficient) can be collected in a vector $\boldsymbol{\theta}_{FG}^T = \left[c_f, p_f, \mathbf{a}^T \middle| \mathbf{c}_b, \mathbf{p}_b\right]$ where $\boldsymbol{a} = [a_1, \ldots, a_L]^T$, and the vectors $\mathbf{c}_b$ and $\mathbf{p}_b$ represent the lexicographically unwrapped, previously estimated Compton and photoelectric images, here assumed to be known. We then solve a simplified version of Eq. 14:

$$\arg\min_{\boldsymbol{\theta}_{FG}} F(\boldsymbol{\theta}_{FG}) = \frac{1}{2}\left(\mathbf{y} - \mathbf{m}(\boldsymbol{\theta}_{FG})\right)\boldsymbol{\Sigma}\left(\mathbf{y} - \mathbf{m}(\boldsymbol{\theta}_{FG})\right)^T + R_{FG}(\boldsymbol{\theta}_{FG})) \tag{28}$$

As regularization terms for this problem, we use

$$R_{FG}(\boldsymbol{\theta}_{FG}) = R_s(\boldsymbol{a}) + R_{prop}(c_f, p_f) \tag{29}$$

The first term is the commonly used penalty term[15,19] that encourages objects of interest to have a small area:

$$R_s(\boldsymbol{a}) = \lambda_1 \| H(\boldsymbol{\mathcal{O}}) \|_1. \tag{30}$$

where $\| \ \|_1$ indicates cardinality, i.e. the number of pixels where $\chi(x, y) = 1$. The second term captures our prior knowledge about the expected physical properties of the objects of interest, and specifies a subset Γ of allowable values for the object values in the (p_f, c_f) parameter space. In general, many chemical compounds of interest may exist, so the set of allowable parameter values could be comprised of a number of disconnected regions. However, for simplicity here we consider the case where the constraint set is elliptical in shape. We define $\Gamma \in \mathcal{R}^2$ as an ellipse with the center (c_0, p_0) major axis σ_p and minor axis σ_c. Then, we can write a non-linear inequality constraint as

$$\frac{(c_f - c_0)^2}{\sigma_c^2} + \frac{(p_f - p_0)^2}{\sigma_p^2} < 1 \tag{31}$$

For numerical solution, we transform this inequality constraint into a penalty term which assigns a cost to violating the constraint above (i.e., penalizes the case when the LHS of Eq. 31 is <1), then solve an unconstrained problem. First we define the term:

$$g_1(p_f, c_f) = \frac{(c_f - c_0)^2}{\sigma_c^2} + \frac{(p_f - p_0)^2}{\sigma_p^2} - 1 \tag{32}$$

then introduce the following penalty term:

$$\begin{aligned} R_{prop}(c_f, p_f) &= \lambda_2 \max\Big(g_1(p_f, c_f), 0\Big) \\ &= \lambda_2\left(\sqrt{g_1^2(c_f, p_f) + \epsilon} + g_1(c_f, p_f)\right) \end{aligned} \tag{33}$$

where on the second line we have introduced a soft (and differentiable) version of the 'max' function.

4.1 Simulation results

Here we present results of the method outlined above on simulated dual-energy data* generated for a suitcase phantom, for geometries typical of airport scanner systems. While our method does not assume parallel beam sinograms *per se*, we chose to work with simulated data for parallel beam geometry (1024 detector positions $\times$ 720 angles, evenly spaced between $0 - 180$ degrees). We note that parallel-beam data is commonly generated by rebinning fan-beam data in commercial scanners, allowing use of the Radon transform for image formation. We added Gaussian noise to the Poisson-distributed simulated data to achieve 60 dB signal-to-noise ratio for electronics noise.

*provided by Dr. Taly Gilat-Schmidt of Marquette University

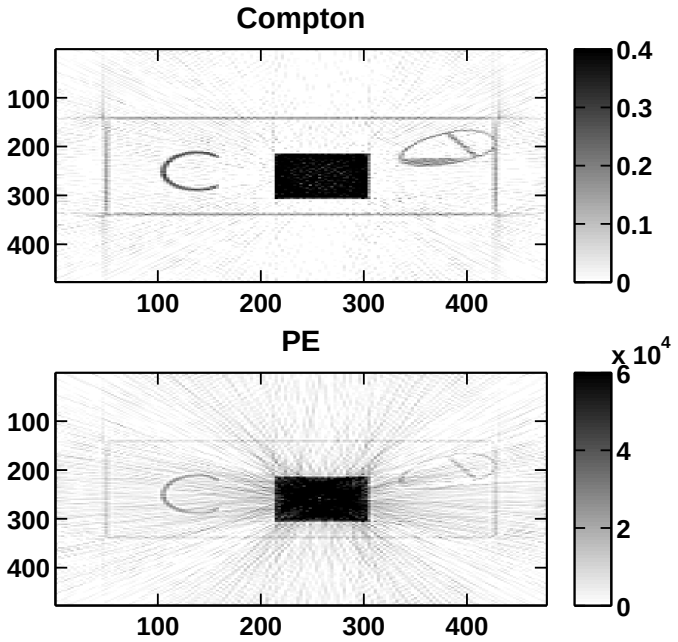

Figure 2. Reconstruction using edge regularization

Figure 2 shows estimated background Compton and PE images from the data, using the (non-convex) edge regularization approach previously studied.[3] Without any regularization, the PE image is extremely noisy (not shown). With the edge-based regularization, a reasonable PE image is obtained, but there is noticeable noise in the image and the outline of the object to the upper right (simulated water bottle) is obscured. In contrast, use of the NLM regularizer, shown in Fig. 3, leads to a much smoother PE estimate. While there is residual "smudge" in the image, this type of smooth variation could be more easily handled by post-processing of the images. In particular, the water bottle outline is much clearer. Note that the Compton images for the two results are quite similar.

One important difference between the two regularizers is that, because the edge-based regularizer encourages PE solutions with similar edges to the Compton image, any streak artifacts in the Compton image will tend to carry over to the PE image. The NLM regularizer, by contrast, encourages averaging during the PE reconstruction of patches that are similar in the Compton image, but is less likely to map streak artifacts from Compton to PE.

An example of foreground estimation is shown in Figure 4. In this case, the material of interest is correctly identified as separate from the background. The outline of the material of interest can be used in subsequent processing, as it provides an automatic segmentation of the object. In this example the 60 dB noise had a significant impact on the background estimates, leading to high variation within the object being imaged. Use of the foreground region estimates improves the match to the data and identifies homogeneous regions, which would aid material identification. The algorithm converged to values of 0.386 cm^{-1} (Compton) and 7.06e3 $KeVcm^{-1}$ (PE), close to the true values of 0.37 and 7.24e3.

In addition to the image stabilization demonstrated in Fig. 4, the foreground\background separation also allows us to use higher spatial resolution for foreground objects, as we can estimate the foreground using a finer-grained basis set. As an example, Fig. 5 shows the CT reconstruction for a low-noise case with the suitcase phantom, zoomed in around the 'C'-shaped object. The foreground estimate is run for only the region around this object. While the background estimates (upper row) are somewhat pixelated ($\mathbf{B}$ consisted of 3×3 pixel blocks in this background estimate run) the foreground model estimate (middle row) is clearly of higher resolution. The lower row shows foreground and background images combined as in Eqns. 6- 7. As can be seen, the background

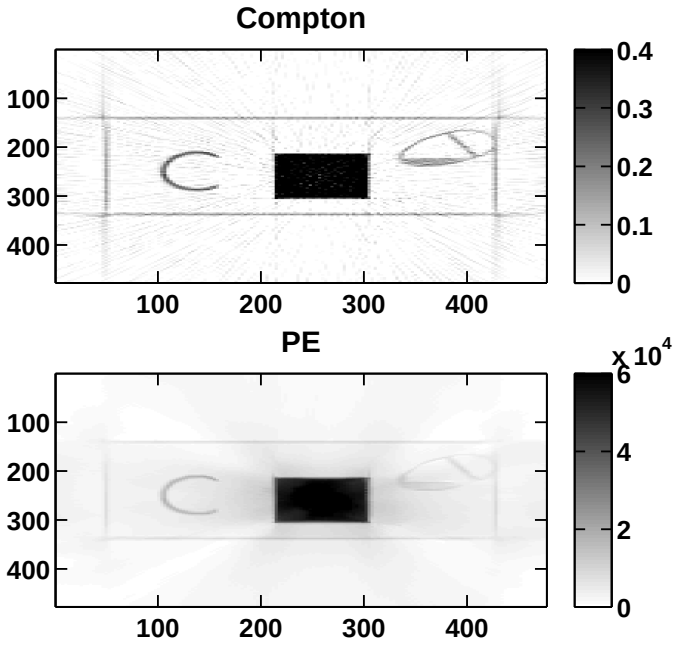

Figure 3. Reconstruction using NLM regularization

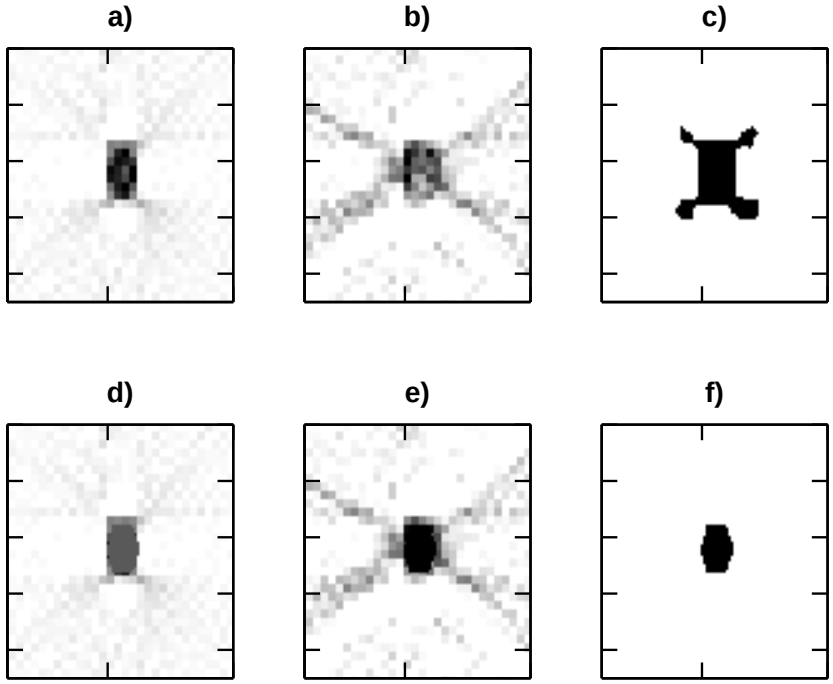

Figure 4. Foreground object estimation using proposed method. a) background Compton estimate; b) background photoelectric estimate; c) starting estimate of object-of-interest location (initial χ); d) final Compton image; e) final photoelectric image; f) final estimate of χ. The stabilized PE image in e) vs. b) can be expected to aid material identification. Compton plot range is $[0, 0.6]cm^{-1}$, and PE plot range is $[0, 1e5]KeVcm^{-1}$.

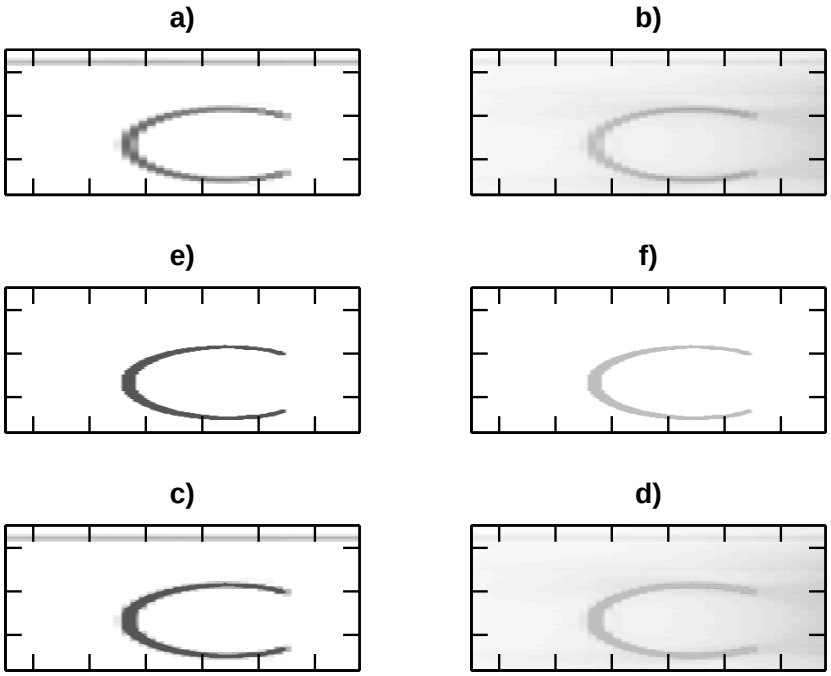

Figure 5. Foreground object estimation using parametric level set method, low-noise case with suitcase phantom. The foreground estimate is run only for a user-specified region sounding the 'C'-shaped object. a) background Compton estimate, showing 'C' and upper edge of suitcase; b) background photoelectric estimate; c) foreground Compton; d) foreground photoelectric; e) Compton image, background + foreground); f) photoelectric image, background + foreground.

estimate contains some residual elements of the 'C'-shaped object, which if desired could be removed by iteratively estimating the background and foreground.

4.2 Discussion

This paper has outlined an iterative image formation approach for dual- and multi-energy CT data. Key features of the approach are that we employ parametric level sets to estimate the outline of materials of interest, providing an ability to form images with enhanced spatial resolution in the most interesting areas, and the use of patch-based regularization techniques to stabilize image reconstruction. The patch-based regularization provides improvements in image quality, as demonstrated here on simulated data, and also allows use of fast, parallelizable solution techniques for convex problems. In ongoing work we are exploring use of these techniques as well as application of the method to real data.

ACKNOWLEDGMENTS

The authors gratefully acknowledge helpful insights provided by Dr. Oguz Semerci and Prof. Taly Gilat-Schmidt, as well as DHS funding provided through the ALERT Center at Northeastern University.

REFERENCES

1. Z. Ying, R. Naidu, and C. Crawford, "Dual energy computed tomography for explosive detection," *J. of X-ray Sci. and Tech.* **14**(4), pp. 235–256, 2006.
2. P. Shikhaliev, "Energy-resolved computed tomography: first experimental results," *Physics in medicine and biology* **53**, p. 5595, 2008.

3. O. Semerci and E. L. Miller, "A Parametric Level-Set Approach to Simultaneous Object Identification and Background Reconstruction for Dual-Energy Computed Tomography," *Image Processing, IEEE Transactions on* **21**, pp. 2719–2734, May 2012.
4. R. Alvarez and A. Macovski, "Energy-selective reconstructions in x-ray computerized tomography," *Phys. Med. Biol.* **21**(5), pp. 733–744, 1976.
5. J. Beutel, *Handbook of medical imaging: Physics and psychophysics*, vol. 1, Spie Press, 2000.
6. R. L. Siddon, "Fast calculation of the exact radiological path for a three-dimensional CT array," *Medical Physics* **12**(2), pp. 252–255, 1985.
7. B. De Man and S. Basu, "Distance-driven projection and backprojection in three dimensions," *Physics in Medicine and Biology* **49**, pp. 2463+, May 2004.
8. J. H. Siewerdsen, M. J. Daly, B. Bakhtiar, D. J. Moseley, S. Richard, H. Keller, and D. A. Jaffray, "A simple, direct method for x-ray scatter estimation and correction in digital radiography and cone-beam CT," *Medical Physics* **33**(1), pp. 187–197, 2006.
9. O. Semerci, *Image Formation Methods for Dual Energy and Multi-Energy Computed Tomography.* PhD thesis, 2012. Tufts University.
10. A. Buades, B. Coll, and J.-M. Morel, "Image enhancement by non-local reverse heat equation," tech. rep., CMLA, 2006.
11. G. Wang and J. Qi, "Penalized likelihood PET image reconstruction using patch-based edge-preserving regularization.," *IEEE transactions on medical imaging* **31**, pp. 2194–2204, Dec. 2012.
12. Y. Wu, B. Tracey, P. Natarajan, and J. P. Noonan, "James stein type center pixel weights for non-local means image denoising," *Signal Processing Letters, IEEE* **20**, pp. 411–414, Apr. 2013.
13. N. Rezvani, *Iterative Reconstrunction Algorithms for Polyenergetic X-ray Computerized Tomography.* PhD thesis, 2012. University of Toronto.
14. S. Osher and R. P. Fedkiw, *Level Set Methods and Dynamic Implicit Surfaces, Applied Mathematical Sciences*, vol. 153, New York: Springer, 2002.
15. T. F. Chan and L. A. Vese, "Active contours without edges," **10**, pp. 266–277, Feb. 2001.
16. O. Dorn, E. Miller, and C. Rappaport, "A shape reconstruction method for EM tomography," *Inverse problems* **16**, pp. 1119–1156, 2000.
17. A. Aghasi, M. Kilmer, and E. Miller, "Parametric level set methods for inverse problems," *SIAM Journal on Imaging Sciences* **4**(2), pp. 618–650, 2011.
18. M. Schweiger and S. Arridge, "Image reconstruction in optical tomography using local basis functions," *Journal of Electronic Imaging* **12**, p. 583, 2003.
19. O. Dorn and D. Lesselier, "Level set methods for inverse scattering," *Inverse Problems* **22**(4), pp. R67–R131, 2006.